How Thermal Fluctuations Influence the Function of the FeMo-cofactor in Nitrogenase Enzymes

Wan-Lu Li
University of California, Berkeley
Yong Li
Uppsala University
Jun Li
Tsinghua University https://orcid.org/0000-0002-8456-3980
Teresa Head-Gordon (thg@berkeley.edu)
University of California, Berkeley https://orcid.org/0000-0003-0025-8987

Article

Keywords:

Posted Date: August 15th, 2022

DOI: https://doi.org/10.21203/rs.3.rs-1960003/v1

How Thermal Fluctuations Influence the Function of the FeMo-cofactor in Nitrogenase Enzymes

Wan-Lu Li[1,3], Yong Li[4,5,7], Jun Li[4,6], Teresa Head-Gordon[1–3]

[1]Kenneth S. Pitzer Theory Center and Department of Chemistry,
[2]Departments of Bioengineering and Chemical and Biomolecular Engineering
University of California, Berkeley, CA, 94720 USA
[3]Chemical Sciences Division, Lawrence Berkeley National Laboratory, Berkeley, CA, 94720 USA
[4]Department of Chemistry, Tsinghua University, Beijing, 100084, China
[5]Institute of Applied and Physical Chemistry and Center for Environmental Research and Sustainable Technology, University of Bremen, Bremen, 28359, Germany
[6]Department of Chemistry, Southern University of Science and Technology, Shenzhen, 518055, China
[7]Department of Chemistry-Ångström Laboratory, Uppsala University, Uppsala, 75121, Sweden
corresponding authors: yong.li@kemi.uu.se; thg@berkeley.edu

Abstract

The catalytic mechanism of N_2 fixation by nitrogenase has been discussed over decades, but still remains unresolved in how the strong N≡N bond is activated and why the reaction requires the reductive elimination of H_2. In this work, we use two different levels of Density Functional Theory (DFT) methods while also considering the influence of statistical fluctuations from finite temperature ab initio molecular dynamics to elucidate the functional mechanism of the complete nitrogenase catalytic cycle. Over the accumulation of four reducing equivalents we show that protons and electrons transfer to the FeMo-cofactor to weaken and break the Fe-S bond that then exposes the Fe coordination sites to physisorb the N_2 molecule. Remarkably, we find that subsequent H_2 formation is responsible for chemical activation to an N=N double bond (up to 0.09 Å elongation) with a low barrier (< 5 kcal/mol) to H_2 release. This greatly eases the hydrogenation step to NH_3 with further H_2S consumption, completing the catalytic cycle of $N_2 + 8H^+ + 8e^- \rightarrow 2NH_3 + H_2$. This work helps explain why H_2 formation is an obligatory and essential step in N_2 adsorption and activation, insight that will inform the design of molecular catalysts and other N_2 reduction reactions.

INTRODUCTION

The nitrogenase enzyme can absorb and activate the strong N≡N triple bond at ambient conditions to catalyze the reduction reaction of N_2 to NH_3, thereby providing a biological fixation route to more than half of the nitrogen needed to sustain the human population on earth[1–5]. The total dinitrogen hydrogenation process, $N_2 + 3\ H_2 \rightarrow 2NH_3$, is net exothermic (enthalpy, -0.47 eV/mol), and more so if activated hydrogen in the form of solvated H^+/e^- is utilized. However, the first bond cleavage of the N_2 molecule requires enthalpy $\Delta H \approx 4.7$ eV at standard temperature and pressure, which is almost one-half the value for full N_2 dissociation (9.7 eV)[6]. Furthermore, the large HOMO-LUMO gap (ca. 10 eV) and the low proton affinity (5.1 eV) of N_2 make the processes of electron and proton transfer to N_2 very difficult at the beginning of the nitrogen fixation reaction. Therefore, there is great interest in the molecular-level understanding of how the nitrogenase enzyme achieves this challenging task. Significantly, elucidating the biological mechanism of nitrogen fixation would also be useful and insightful in the development of more efficient catalysts for industrial ammonia synthesis.

The FeMo cofactor (FeMo-co) in a hetero-tetrameric 'MoFe protein' of nitrogenase (Fig. 1a) is the functional catalytic unit with a triangular prism Fe_7MoCS_9 cluster that utilizes supplied electrons and protons (from $(H_2O)_nH^+$ chains[9]) to reduce the N_2. The stoichiometry of the nitrogenase-catalyzed nitrogen fixation under ambient conditions is experimentally identified by the reaction in Eq. (1)

$$N_2 + 8H^+ + 8e^- + 16ATP \rightarrow 2NH_3 + H_2 + 16ADP + 16Pi \tag{1}$$

where ATP, ADP, and Pi are the metabolites adenosine triphosphate, adenosine diphosphate, and an inorganic orthophosphate, respectively.[8] Utilizing the energy released from the hydrolysis of coenzyme ATP, the electrons are transferred from the Fe protein to the MoFe protein, where NH_3 and obligatory H_2 are generated on the FeMo-co subunit[1,10,11]. The Lowe-Thorneley (LT) model[8] describes the transformations and kinetics among catalytic intermediates (denoted $\mathbf{E}_n$) for which eight H^+/e^- reducing equivalents delivered to the FeMo-co center ultimately create the NH_3 reductive product (Fig. 1b). The LT model

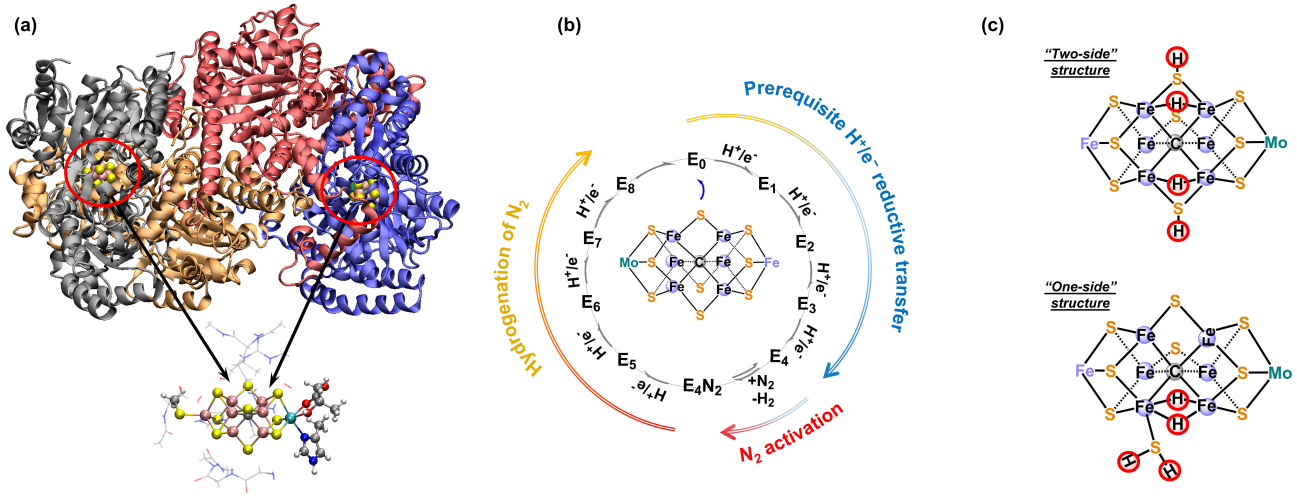

Figure 1: *The nitrogenase enzyme and FeMo-co unit used to execute the catalytic steps for nitrogen fixation over a complete cycle.* (a) the MoFe protein (PDB ID: 3U7Q)[7] with FeMo-co center highlighted in the ball and stick model below. (b) The whole catalytic cycle of nitrogen fixation by nitrogenase from steps $\mathbf{E}_1$ to $\mathbf{E}_8$ based on the Lowe-Thorneley kinetic model[8]. Further details are provided in Supplementary Materials S1. (c) The FeMo-co structures of the two-side (2S) and one-side (1S) configurations for the $\mathbf{E}_4$ state. The adsorbed H atoms are circled in red.

assumes that ten main intermediates are involved in the entirety of nitrogen bio-fixation reactions, although the detailed reaction mechanism might contain even more intermediates for H^+/e^- pair transfers, N_2 activation, H_2 formation, N_2 protonation, and NH_3 production. Experimental studies have revealed that the cofactor in the MoFe protein can exist in three states: the resting or native state (FeMo-co^N), the one-electron reduced state (FeMo-co^{Red}), and the one-electron oxidized state (FeMo-co^{Ox})[1]. It is of primary importance to determine the relations between these three experimentally identified states of the LT kinetic scheme.

Despite the numerous experimental efforts that have been carried out to explore nitrogenase and its catalytic mechanism, there are no crystallographic structures of any $\mathbf{E}_1$ to $\mathbf{E}_8$ intermediates such as the bound -N_2- species or hydrogenated -N_2H_x- states due to their labile nature, and thus many mechanistic aspects of the nitrogenase-catalyzed N_2 fixation reaction remains unknown[1,2,11]. Therefore theoretical investigations to explore and identify the possible activated species and intermediates in the nitrogenase cycle have become essential to fully understand the mechanism[2]. Neese and Bjornsson have thoroughly uncovered the electronic structure of FeMo-co using quantum chemical calculations along with experimental measurements, including the oxidation states of Mo and Fe centers, net charges, and its magnetic properties have been widely reported[3,12–14]. The prerequisite protonations of FeMo-co and the hydrogenation of N_2 have been reported in the theoretical literature based on chemical models that typically rely on Density Functional Theory (DFT).[15] Using the BP86 GGA functional[16], Hoffman and co-workers proposed an $\mathbf{E}_4$ state with a "two-side" (2S) structure (Fig. 1c), where the adsorption sites of hydrogen atoms occur on both sides of the bridged sulfurs[17–19], to create a weakly physisorbed N_2[17]. Using a hybrid functional, Siegbahn has argued that the mechanism with hydrogenation of the central C atom is energetically more favorable so that the formation of CH_3 at $\mathbf{E}_4$ can provide a cavity for N_2 binding (see also the Supplementary Materials). Ryde's group carried out systematic calculations with different exchange-correlation functionals especially for the N_2 hydrogenation steps[20–22]. However, the reason why H_2 formation is crucial and obligatory and the detailed N_2 activation steps, in particular the creation of the activated N=N double bond[19,20,23], are still open research questions. A new clue in the nitrogenase story is a report that the HS^- species can be removed from its bridge site and binding to the Gln-176 residue in V-nitrogenase[24], setting up the possibility of dissociation of bridged S from FeMo-co as recently discussed by us and others[25,26].

In addition to choice of exchange-correlation functional, the greater environment of the protein is required beyond an isolated FeMo-co catalytic center. Raugei et al. have developed an extended cluster model of FeMo-co within a corona of amino acids[27], showing that it is a necessary ingredient when considering the energetics of the $\mathbf{E}_4$ state in particular. Moreover, nitrogenase operates it's catalytic function under ambient temperature, and therefore thermal motions might influence the energetic stability of various intermediates that is crucial to understand and reveal the catalytic mechanism of the total reaction profile[28,29]. We wish to especially acknowledge the fact that all enzymes exhibit low activity at cold temperatures and are only fully active at an optimal finite temperature. For example, thermally averaged motions found from room-temperature X-ray crystallography have been shown to be important for enzyme catalysis[27], and statistical fluctuations of active site residues are productively utilized for enzyme turnover events for Ketosteroid isomerase[30], add further nuance to pre-organized electric fields[31,32] as well as effecting the catalytic barrier[33]. However, to the best of our knowledge, no study has examined the effect of thermal fluctuations on the entire FeMo-co catalytic mechanism for nitrogenase.

Based on an extended cluster model of FeMo-co that includes directly contacting protein residues[27], with an implicit solvent environment beyond that, we consider the energetics of the LT kinetic model of the complete cycle[8] using *ab initio* molecular dynamic (AIMD) and metadynamic simulations, with two different DFT functionals to ensure that conclusions are consistent across quantum mechanical models. Only when we consider a statistical thermodynamic perspective do we find that both functionals (Meta-GGA-B97M-rV and GGA-BP86) independently and consistently predict a "one-side" (1S) mechanism (Fig. 1c), i.e. H adsorption occurs on the same side of bridged sulfurs with subsequent H_2S formation, which is conducive

to exposing two Fe coordination sites to subsequently adsorb N_2. Remarkably, the accounting of thermal motion lowers the barrier to H_2 release that then activates the N_2 triple bond to undergo a chemical change to a double bond, thereby explaining why H_2 is an obligatory step in the nitrogenase enzyme mechanism.

RESULTS AND DISCUSSION

The $\mathbf{E}_0$ state is proposed to have a net charge of -2 with an oxidized form of FeMo-co^{Ox} and a protonated hydroxyl group, based on extensive analysis of the oxidation and spin state of FeMo-co described thoroughly in the Supplementary Materials and Supplementary Figures S1 and S2. Based on the FeMo-co cluster model by Raugei et al. as shown in Fig. 2a[27], the BP86 functional yields the lowest mean absolute deviations (MADs) for the geometric parameters of the $\mathbf{E}_0$ state (Fig. 2b) at both 0 K and 300 K compared with experiment[7], supporting its popularity for describing metallo-enzymatic systems[17]. The semiempirical meta-GGA functional B97M-rV[34,35] has also shown promise by correctly describing the intermolecular interactions of many molecular systems[36–38] and has accurately predicted surface relaxations and CO adsorption energies for precious metal electrocatalysts consistent with experimental findings in the NVT ensemble[28]. Therefore, we also considered the B97M-rV performance on the same metalloenzymatic system for the full LT catalytic cycle. We find that the calculated bond lengths in the FeMo-co center for $\mathbf{E}_0$ using B97M-rV are overestimated but with a MAD that is acceptable upon inclusion of thermal effects (0.076 Å), a correction that is especially dramatic for the Mo bonds.

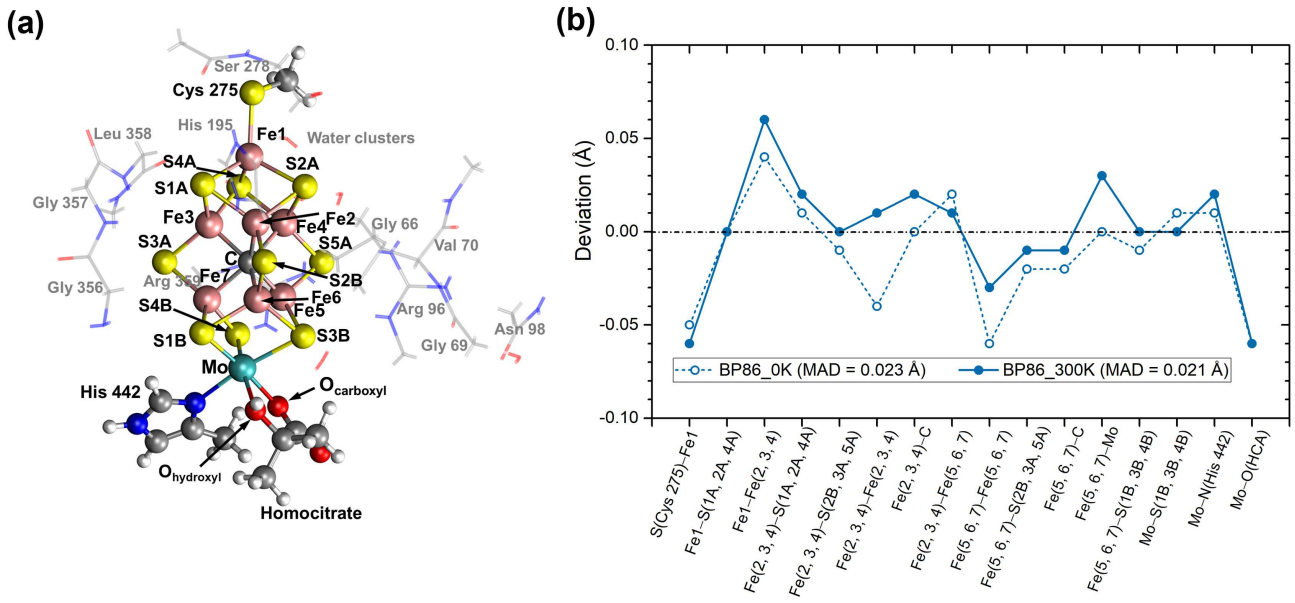

Figure 2: *The FeMo-co computational model and agreement between the bonded structure of the* $\boldsymbol{E}_0$ *state from BP86 and experiment.* (a) The cluster model, with an extended protein environment of FeMo-co due to Raugei and co-workers[17] in the context of the surrounding key residues (labels in grey). Color code: H-white, C-gray, N-blue, O-red, S-yellow, Fe-lilac, Mo-cyan. (b) Bond-length deviations calculated at the level of BP86, with and without thermal statistics, compared to the PDB structure (PDB ID: 3U7Q)[7]. The Mean Absolute Deviations (MAD) values are shown in parentheses. Similar calculations using the B97M-rV functional are provided in Supplementary Table 2.

Prerequisite H^+/e^- reductive transfers before N_2 activation

The first four protonation processes of H^+/e^- pair-transfers to the FeMo-co center have been suggested to be the preparation for N_2 binding[1,39,40]. Although the possible protonated structures for $\mathbf{E}_1$ through $\mathbf{E}_4$ have been reported previously[17,41,42], it is still debatable as to which is the most energetically stable structure at each E_n step. In addition, the [Fe-H-Fe] metal-hydride bonds in some organometallic catalysts have been reported to play a key role in the adsorption and activation of the N_2 molecule[6], and also found to be relevant for the FeMo-co structure by ^{1,2}H and ^{95}Mo ENDOR experiments[43,44]. But because FeMo-co is a quasi-symmetric triangular prism with three facets for reactions, what is the hydride structure formed during the early H^+/e^- transfer stages is not fully known, although experimental mutation studies have implicated that hydride adsorption occurs on a single facet, "f1", defined by Fe2-S2B-Fe6-S5A[45–47].

The structure of the key $\mathbf{E}_4$ state[11,23,48,49] has been called the "Janus intermediate" since it has been experimentally suggested to contain two [Fe-H-Fe] bridging hydrides and can react in both directions for releasing H_2 or desorbing N_2[1,5,44]. Yet, it has not been possible to deduce an unambiguous picture of the spatial relationships of the two hydride bridges by experiment[1,5], and therefore theoretical studies have become essential to fill in this structural picture. The decision of whether the H adsorption occurs on a 1S *vs* 2S structure of the bridged sulfurs (Fig. 1c) can lead to a dramatically different conclusion regarding N_2 activation and H_2 release. All previous studies concerning the $\mathbf{E}_4$ state have exclusively predicted a 2S configuration[17,49].

Our computational results using BP86 consistently finds the first protonation at $\mathbf{E}_1$ occurs at the sulfide atoms between two Fe sites in the f1 facet regardless of temperature, and weakening the Fe-S bonds within each face (Fig. 3), which is well consistent with the K-edge EXAFS finding[50]; similar conclusions are reached using B97M-rV at finite temperature (Supplementary Fig. 4). Proceeding to the $\mathbf{E}_2$ step, both DFT functionals at 0 K prefer the proton adsorption onto another bridging sulfide forming a 2S configuration, while the 1S configuration with one [Fe-H-Fe] has a higher energy by > 0.8 eV (Fig. 3a, Supplementary Fig. 4). Hoffman and coworkers[17,19] also found the same 2S structure for the $\mathbf{E}_4$ state. However, there must be an obligate side-crossing of hydrogen from S5A to the S2B site which would have to surmount a barrier of over 1 eV as demonstrated for the metadynamics simulation in Fig. 3b for the $\mathbf{E}_3$ state; one would imagine the same large barrier would be present in the 4^{th} proton transfer of the $\mathbf{E}_4$ state.

We determine that at 300 K both functionals exclusively prefer the 1S configuration path, which induces a more stable adsorption on the bridging [Fe-H-Fe] site due to the relaxation of the sterically hindered repulsion that increased the energy of the 1S structure at 0 K. As a result, the formation of [Fe-H-Fe] for the $\mathbf{E}_2$ step weakens the Fe←$(SH)^-$ bond (Fig. 3c) such that the 1S structures for hydride transfer at the $\mathbf{E}_3$ and $\mathbf{E}_4$ stages completely unfolds the Fe6 site with the formation of H_2S and two [Fe-H-Fe] bonds. This leads to complete exposure of the Fe6 coordination site for N_2 adsorption. Notably, the temporary generation of the H_2S starting from $\mathbf{E}_3$ promotes the exposure of the iron coordination site but will not break the catalytic cycle. Since the complete nitrogenase environment contains residues that can hold H_2S via noncovalent interactions[51], and water chains that are connected through the homocitrate ligand continuously supply transferred protons hydrolyzing H_2S into HS^- and H_3O^+, helps justify this mechanism. This conclusion is also supported by a recent crystal of V-nitrogenase[24] that showed that an HS^- ion can bind in a holding site of the rearranged protein residue Gln-176 preventing its complete removal from the VMo-co. Because the accumulation of H^+/e^- on FeMo-co requires a combination of protonation and electron-transfers, we independently evaluated the proton-coupled electron transfer (PCET)[52,53] process for nitrogenase catalysis in this work. Our calculated ionization energies and proton affinities of structures from E_0 to E_4 shows that the proton and electron transfer reactions depend on and promote each other (as discussed in Supplementary Information S1.2), confirming that the concerted PCET is energetically favorable.

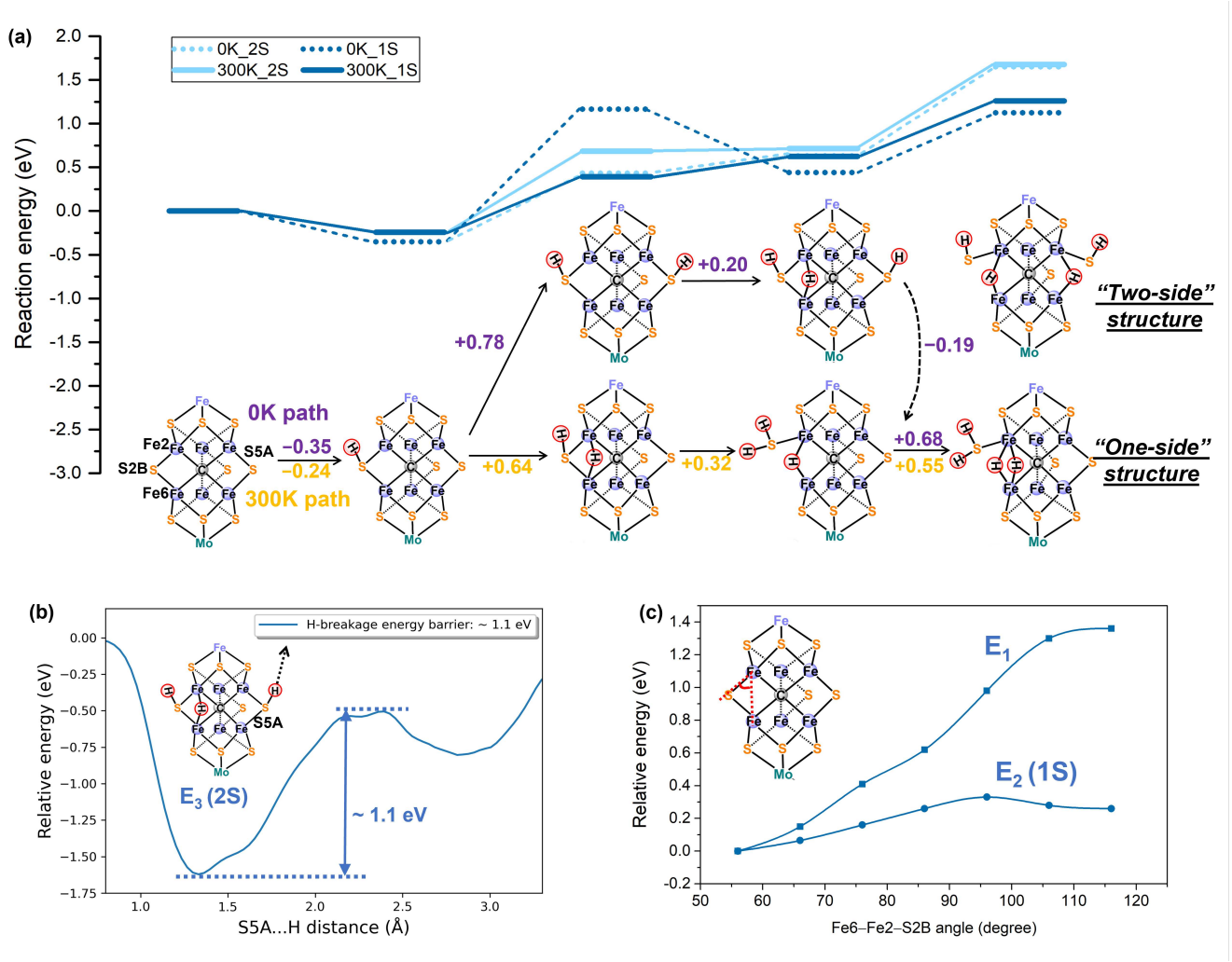

Figure 3: *Reaction path of the prerequisite H^+/e^- transfers.* (a) Energy profile of the H^+/e^- transfer path from $\mathbf{E}_0$ to $\mathbf{E}_4$ predicted by the BP86 functional at 0 K and 300 K. 2S and 1S structures are plotted in the first and second row, respectively. Energy differences at 300 K are calculated as the statistically averaged values. The minimum energy paths are highlighted in purple (0 K) and yellow (300 K). The dash lines represent the energy cost of 1S to 2S crossings. (b) One-dimensional free energy surface from a metadynamics simulation at 300 K, describing the H dissociation from the S5A site of the 2S structure at the $\mathbf{E}_3$ stage, indicating the energetic cost to cross from 2S to 1S is large. A similar set of results for the B97M-rV functional is provided in Supplementary Fig. 4, and results for the other higher energy paths for facets 2 and 3 are given in Supplementary Fig. 5. (c) Energy scans of Fe-S bond cleavage along the bond angle of Fe6-Fe2-S2B at $\mathbf{E}_1$ and $\mathbf{E}_2$ (1S) stage, respectively. We are unable to obtain the energy curve of the $\mathbf{E}_0$ due to the difficulty of SCF convergence but the bond cleavage is estimated to be larger than 2.5 eV. The Fe-S bond cleavage becomes easier (less than 1.32 eV) when the S vertex is protonated. However, the Fe-S bond cleavage is facile to achieve after another proton transfers to the bridge of Fe2 and Fe6, with only a ∼0.35 eV barrier and ∼0.21 eV dissociation energy. This calculation is done at 0 K as we do not expect a qualitative change at 300 K due to the dramatic decrease of the dissociation energy in $\mathbf{E}_2$ compared with that in $\mathbf{E}_1$ (> 1 eV).

Activation of N_2 and H_2 release

As determined above, the Fe6 site is completely exposed after the fourth proton transfer to FeMo-co, creating two bridged [Fe-H-Fe] bonds that are a favorable site for the adsorption of the N_2 molecule. Here we use metadynamics within the collective coordinates that capture the adsorption and activation process in Figure 4. We find that N_2 absorbs onto the exposed Fe site of the $\mathbf{E}_4$ state via an $\mu_1 - \eta^1$ end-on mode (Figs. 4a and 4b), with a corresponding adsorption energy of -0.21 eV at 300 K (-0.35 eV at 0 K, implying physical adsorption), and some small activation is present by bond elongation ∼0.04 Å (Fig. 4c).

From the metadynamics simulation we also determine an intermediate $\mathbf{E}_4\mathbf{N}_{2\_IM}$ state which has a H_2-bound configuration that is consistent with recent photophysical experimental measurements[54]. From the intermediate state there is a low ∼ 3 kcal/mol energy barrier for release of H_2, which in turn stabilizes the adsorption of N_2 by more an 0.5 eV (implying a change from physical to chemical adsorption) by allowing it to form an interaction with the two Fe atoms, defined as the $\mu_2 - \eta^2$ configuration (Fig. 4b). Apparently, H_2 formation greatly enhances the N_2 binding from a weak physical adsorption to a stronger chemical adsorption and further breaking its triple bond (see below), thus answering the long-standing unanswered question as to why H_2 formation is obligatory and how N_2 was activated[55]. Interestingly, this structure is in good agreement with the recent experimental observation of a synthetic [Mo_3S_4Fe] cube[56], which proposed that the N_2-reduction capability of Fe atoms is enhanced in a sulfur-rich environment. Overall the $\mu_2 - \eta^2$ state is somewhere between end-on and side-on configurations, a point to which we return to in the next Section.

At both 0 and 300 K, the bond length of N_2 dramatically elongates by 0.09 Å in the bound $\mu_2 - \eta^2$ state relative to the free gaseous N_2 molecule, indicating the effective activation of N≡N to a formal N=N double bond according to the bond order (BO) indices in Fig. 4b and 4c. Therefore, we conclude that the temporary dissociation of H_2S is necessary to fully expose the coordination site of Fe2/Fe6, increasing the N-Fe binding energy that in turn weakens the N_2 bond as illustrated by the longer N...N distance. Although our results using the B97M-rV functional predicts a slightly different reaction sequence between the activation of N_2 and H_2 release (Supplementary Fig. 6), the outcome generated is the same, i.e. where we find that N_2 is efficiently activated based on the observed bond elongation by ∼0.05 Å.

To further support these points, we performed chemical bonding analyses for the N_2 activated structures of $\mathbf{E}_4\mathbf{N}_2$ and $\mathbf{E}_4\mathbf{N}_2^{'}$ predicted using the BP86 functional, illustrating the change of the electronic structure responsive to the adsorption conformations during the activation process. Wiberg bond order (BO)[57] indices and Weinhold effective atomic charges from natural population analysis (NPA)[58] are listed in Supplementary Table 3. The formal triple bond of the free isolated N≡N molecule has a BO = 3.00, and it is further effectively converted into a double bond (BO = 2.24, see also Fig. 4) via electron back-donation from the adjacent Fe6 and Fe2 atoms. From the NPA charges, and despite the low electronegativity (EN) of iron (EN = 1.6 eV, while S and C have EN = 2.4 to 2.5 eV), the Fe atoms are negatively charged in the FeMo-co because of the formal C^{4-} unit at the center, which indicates the importance of the highly anionic carbon in the middle of a slightly deformed Fe6 octahedron to stabilize the geometrical skeleton[59] as well as to modulate electron transfers. The N...N π type bonding orbitals and its π^* antibonding counterparts are shown in Supplementary Fig. 7. From $\mathbf{E}_4\mathbf{N}_2$ to $\mathbf{E}_4\mathbf{N}_2^{'}$, the back-donation of electrons from the 3d-shells is enhanced, coming from the two adjacent Fe sites, thus the total π^* antibonding occupation increases up to 0.5 e. This effectively activates the N≡N triple bond and changes the electronic charge density rearrangement to –N=N.

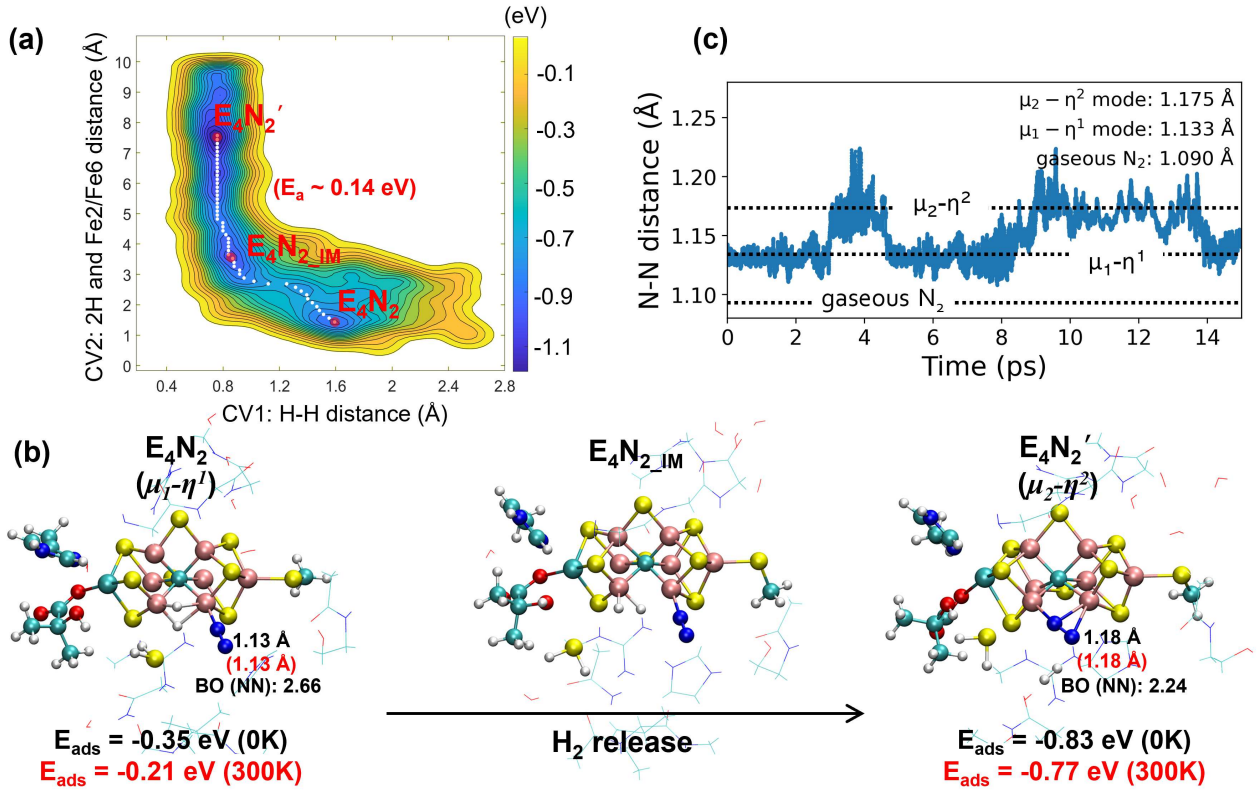

Figure 4: *N_2 adsorption and subsequent H_2 release using AIMD metadynamics simulations with the BP86 functional.* (a) a 15 ps metadynamics simulation, with at least five recrossings among the wells locating the main N_2 adsorption configurations and energetics. The minimum energy paths were calculated using the zero-temperature string method[60] and the activation barrier value is in parentheses. (b) The main configurations along the N_2 activation path: the end-on configuration of $\mathbf{E}_4\mathbf{N}_2$ ($\mu_1 - \eta^1$), the intermediate state $\mathbf{E}_4\mathbf{N}_{2\_IM}$, and the pseudo-side-on configuration of $\mathbf{E}_4\mathbf{N}_2'$ ($\mu_2 - \eta^2$) as evaluated with metadynamics. Adsorption energies are calculated based on the total energy difference relative to $\mathbf{E}_4$ state under both 0 K (black) and 300 K (red). (c) The evolution of the N...N distance showing N_2 activation compared to the gas phase. Wiberg bond order indices are listed here for a quantitative comparison.

Hydrogenation steps after N_2 activation

A number of proposed mechanisms for N_2 reduction have been classified as dissociative and associative (alternating and distal) routes involving the end-on configuration[61], as well as the "enzymatic pathway" involving the side-on configuration.[62] Because there is some ambiguity of the pseudo side-on *vs* pseudo end-on configuration of the $\mathbf{E}_4\mathbf{N}_2'$ state, we must consider the full catalytic cycle by evaluating the $\mathbf{E}_5$ to $\mathbf{E}_8$ steps to best classify the N_2 reduction reaction of the nitrogenase enzyme.

Starting from the fully activated dinitrogen $\mathbf{E}_4\mathbf{N}_2'$ structure, the dissociative pathway of N_2 fixation was excluded since a potential energy surface scan of the cleavage of the N=N double bond on the FeMo-co center yields a very high barrier of ~1.72 eV. Instead, the transferred H^+/e^- pair at the $\mathbf{E}_5$ step hydrogenates the activated -N=N- species at the terminal N atom, forming an -N=N-H intermediate at both 0 K and room temperature consistent with the associative mechanism.

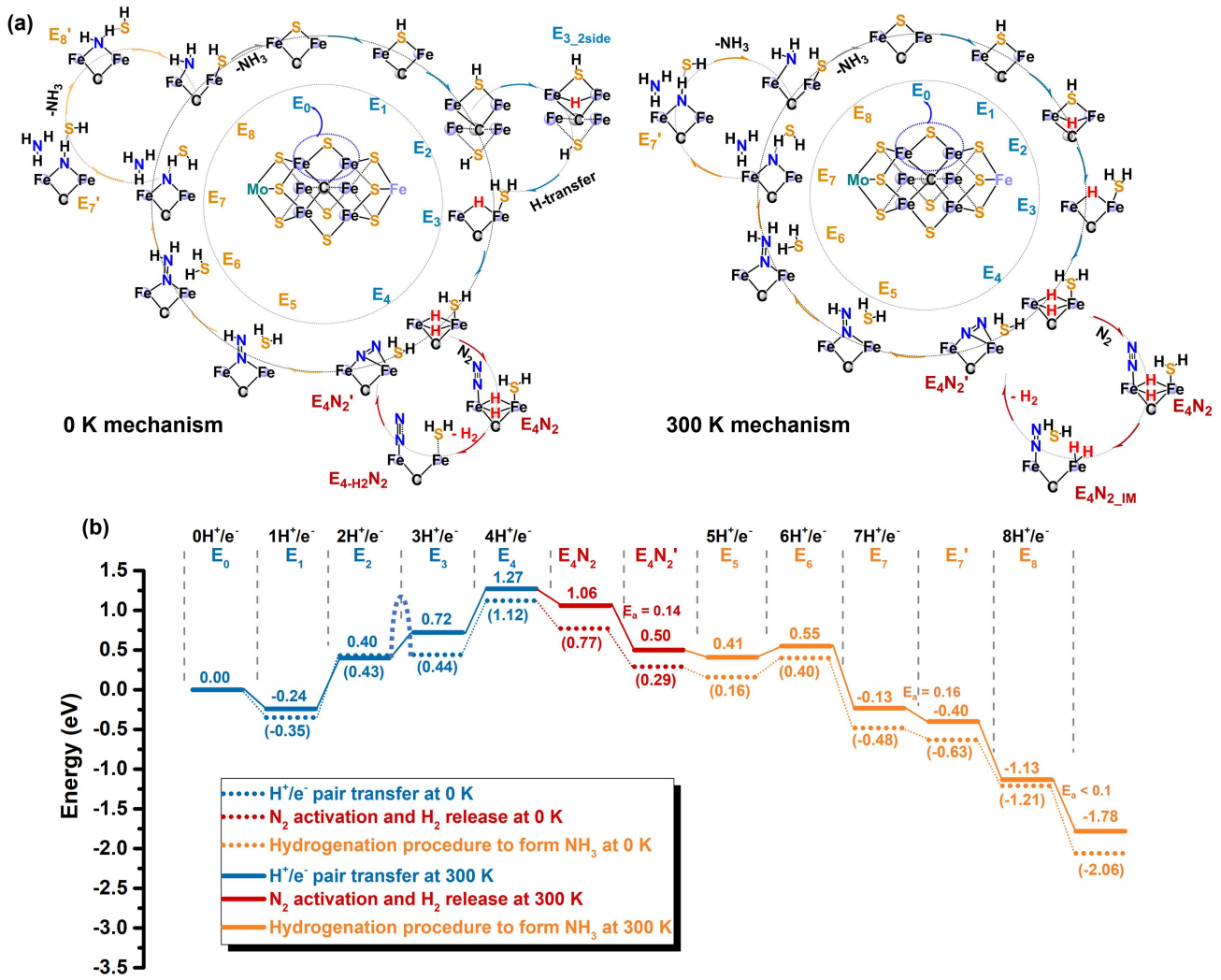

Figure 5: *The whole catalytic cycle of nitrogen fixation by nitrogenase.* (a) Active site geometries during the catalytic cycle at 0 K and 300 K obtained from the BP86 DFT functional. (b) The corresponding energy profiles at 0 K and 300 K for the three processes considered here: H^+/e^- pair transfers (blue), N_2 activation and H_2 release (red), and hydrogenation to form NH_3 (yellow). The bent dotted curve implies the energetic cost of H-transfer to cross from r of the corresponding procedure under 300 K. Details of the reaction energy calculations are provided in the Methods section and Supplementary Materials S1. The catalytic cycle from the B97M-rV functional is provided in Supplementary Fig. 8.

The next hydrogenation step at $\mathbf{E}_6$ is slightly less preferable, requiring 0.24 eV and 0.14 eV at 0 K and 300 K, respectively, forming the -N=NH_2 intermediate consistent with the associative distal mechanism. A potential energy scan of the alternating associative path of NH-NH_2 formation was evaluated as well, and was found to be unfavorable by +0.56 eV compared to the associative distal path forming -N-NH_3. The first NH_3 molecule is then spontaneously generated after one H^+/e^- pair transfer at $\mathbf{E}_7$ with a large amount of heat released, independent of functional or temperature. At this point, the other bridged N atom between the two Fe centers interacts with the H atom of the H_2S moiety, transforming from a hydrogen bond into a stronger covalent N-H bond in the $\mathbf{E}_7'$ state, with an energy barrier of 0.16 eV, cleaving a HS^- species (Fig. 5a). The last H^+/e^- pair is transferred at $\mathbf{E}_8$ to the bridging N and forming an -NH_2 intermediate

species. There exists a shallow intermediate at 0 K ($\mathbf{E}_8'$), but it is eliminated at finite temperature such that the HS^- species directly coordinates back to the Fe2 atom. In the final step, the H atom from the -SH ligand transfers to -NH_2 generating the second NH_3 molecule, the barrier of which is less than 0.1 eV, and resetting the catalytic cycle after the final turnover, where H_2 and NH_3 are released with a product ratio of 1:2. Based on the energy profile in Fig. 5b, we find that once $\mathbf{E}_4$ is formed, the hydrogenation steps from $\mathbf{E}_5$ to $\mathbf{E}_8$ exhibit almost complete exothermic behavior for each of these transformation steps.

CONCLUSION

Using two different levels of DFT theory, and more importantly, the statistical fluctuations of the FeMo-co reaction center at finite temperature, we have generated a well-supported mechanism over the entire catalytic cycle of nitrogenase. Overall the BP86 and B97M-rV support the same mechanism except the latter functional yields an extra step at the $\mathbf{E}_4$ stage, where N_2 can only be adsorbed after H_2 release, but nonetheless elongates the nitrogen bond by 0.05 Å. Regardless of DFT functional, thermal effects in particular yield a different result then found at 0 K by first favoring hydride adsorption on the f1 facet with a 1S configuration that (1) circumvents the side-crossing cost of H atom transfer of the 2S hydride adsorption, and (2) also weakening the Fe-SH bond to more readily form H_2S in $\mathbf{E}_3$. Finally, two such [Fe-H-Fe] hydrides formed in $\mathbf{E}_4$ leads to a complete exposure of the Fe6 coordination site for the subsequent N_2 adsorption regardless of DFT model.

Nonetheless, the BP86 level of theory appears to be in more quantitative agreement with experiments overall, and provides a compelling view of not only N_2 adsorption but a chemically activated N_2 bond. In particular it predicts an N_2 pre-adsorption mode from the $\mu_1 - \eta^1$ state which weakens the N≡N bond (1.09 to 1.13 Å), and after H_2 release is subsequently activated through a highly exothermic $\mu_2 - \eta^2$ bound state that induces a chemical change, reducing the bond order to near 2.2 as the bond length increases further from 1.13 to 1.18 Å. The creation of the H_2S molecule is never observed in the LT mechanism as it can be hydrolyzed into HS^- and H^+ via a water microenvironment, and held in a holding site of the rearranged protein residue Gln-176 to prevent its complete removal from the FeMo-co[24]. Once the vital step of N_2 activation is fulfilled, the following hydrogenation steps from $\mathbf{E}_5$ to $\mathbf{E}_8$ come about naturally to form two NH_3 molecules, while demonstrating a highly exothermic process at the completion of the catalytic cycle.

In summary, this work provides a thorough catalytic mechanism of nitrogenase upon full consideration of the detailed fluctuations of a complete statistical mechanical ensemble: the accumulation of H^+/e^- pairs on the S and Fe sites of FeMo-co for ($\mathbf{E}_0$ to $\mathbf{E}_4$), the necessity of H_2 formation to promote not just N_2 physical adsorption but its chemical activation, and the subsequent hydrogenation of the activated N_2 to form NH_3 ($\mathbf{E}_5$ to $\mathbf{E}_8$). We believe that further enlightening the catalytic pathway in nature's best catalysts is often the best approach to improving synthetic catalysts[29,63], including those that aim to optimize other nitrogen fixation reactions.

METHODS AND MODELS

Based on the FeMo-co cluster model shown in Fig. 2a, we first optimized the geometrical structures with implicit solvent approximated by the COSMO method. Pure GGA-BP86[16,64] and dispersion corrected meta-GGA functional B97M-rV[35] were employed, with optimized small-core GTH pseudopotential[65–67] and the corresponding TZVP MOLOPT basis sets[68] as implemented in CP2K software[69,70]. In all calculations, we used 5 grids for the integral accuracy and the truncated α-C atoms were fixed during the optimization and molecular dynamic simulations. During the geometry optimizations, the convergence criteria were set as 3×10^{-3} bohr for atomic displacements and 4.5×10^{-4} hartree/bohr for the forces.

The electronic structure and spin state determination of $\mathbf{E}_0$, and chemical bonding analyses were performed with the Gaussian 09 D.01 software package[71] for the BP86 functional along with 6-311+G* basis sets for C, N, O, and H, and 6-311+G(2d,p) for S atom[72]. In terms of the heavier elements, effective core pseudo-potentials (ECP)[73] were used with ECP10MDF for Fe, and ECP28MWB for Mo, together with triple-zeta basis sets[74]. The broken-symmetry (BS) method was also used to elucidate the electronic structure of BS7, consistent with the cluster-model calculation mentioned above. The stability of the single-determinant Kohn-Sham-DFT (KS-DFT) wave function was evaluated to ensure that the obtained KS-DFT wave function corresponds to an energy minimum and not a saddle point at low spin states[75,76].

To calculate the adsorption energies of each state at 300 K, we performed AIMD simulations with the timestep of 0.5 fs in the NVT ensemble with a box size of 30 × 30 × 30. Statistical average values were collected over 5 ps with 1 ps equilibration, where the convergence was determined by the energy fluctuation less than 0.2 kcal/mol per atom. The corresponding time-averaged adsorption energy is calculated as Eq. (2).

$$\langle \triangle E_{ads,n} \rangle_{300K} = \langle E_n \rangle_{300K} - \langle E_{n-1} \rangle_{300K} - \frac{1}{2} \langle E_{H_2/N_2} \rangle_{300K} \tag{2}$$

To calculate free energy barriers, we performed well-tempered single walker metadynamic simulations[77,78] for as long as 15 ps using the CP2K package. Two collective variables (CVs) were picked to reduce the dimension of reaction space: (i) the distance between two bridged H atoms of [Fe-H-Fe] and (ii) the distance between the center of two bridged H atoms and the center of Fe2 and Fe6 sites. A wall with the position at 5 angstrom was set for the second collective variable to avoid the complete dissociation of H_2 which is hard to make the reaction backward to sufficiently sample the wells on free energy surface. In the metadynamic calculation, Gaussian functions with 0.002 Hartree height were deposited at least every 30 steps to introduce a bias to introduce a bias in reaction space. The minimum energy path was obtained using the zero-temperature string method proposed by Maragliano and co-workers[60]. We employed the forward Euler approach to capture the overdamped dynamic properties of the string snapshots in the CV 2D space as Eqs. 3 and 4:

$$(CV_1)_i = (CV_1)_{i+1} - h \bigtriangledown_{CV_1} F \tag{3}$$

$$(CV_2)_i = (CV_2)_{i+1} - h \bigtriangledown_{CV_2} F \tag{4}$$

where h = 1×10^{-3}, F is corresponding to the free energy surface. The algorithm was performed in Matlab package using a 50 point string joining the local minima and 2000 optimization steps. The convergence is set to be 1×10^{-5}. Further details and discussion of the computational models are provided in the Supplementary Information.

References

[1] Hoffman, B. M., Lukoyanov, D., Yang, Z.-Y., Dean, D. R. & Seefeldt, L. C. Mechanism of nitrogen fixation by nitrogenase: The next stage. *Chem. Rev.* **114**, 4041–4062 (2014).

[2] Dance, I. Computational investigations of the chemical mechanism of the enzyme nitrogenase. *ChemBioChem* **21**, 1671–1709 (2020).

[3] Van Stappen, C. *et al.* The spectroscopy of nitrogenases. *Chem. Rev.* **120**, 5005–5081 (2020).

[4] Tanifuji, K. & Ohki, Y. Metal–sulfur compounds in N_2 reduction and nitrogenase-related chemistry. *Chem. Rev.* **120**, 5194–5251 (2020).

[5] Seefeldt, L. C. *et al.* Reduction of substrates by nitrogenases. *Chem. Rev.* **120**, 5082–5106 (2020).

[6] Jia, H.-P. & Quadrelli, E. A. Mechanistic aspects of dinitrogen cleavage and hydrogenation to produce ammonia in catalysis and organometallic chemistry: relevance of metal hydride bonds and dihydrogen. *Chem. Soc. Rev.* **43**, 547–564 (2014).

[7] Spatzal, T. *et al.* Evidence for interstitial carbon in nitrogenase FeMo cofactor. *Science* **334**, 940–940 (2011).

[8] Simpson, F. B. & Burris, R. H. A nitrogen pressure of 50 atmospheres does not prevent evolution of hydrogen by nitrogenase. *Science* **224**, 1095–1097 (1984).

[9] Dance, I. The pathway for serial proton supply to the active site of nitrogenase: enhanced density functional modeling of the Grotthuss mechanism. *Dalton Trans.* **44**, 18167–18186 (2015).

[10] Rutledge, H. L. & Tezcan, F. A. Electron transfer in nitrogenase. *Chem. Rev.* **120**, 5158–5193 (2020).

[11] Einsle, O. & Rees, D. C. Structural enzymology of nitrogenase enzymes. *Chem. Rev.* **120**, 4969–5004 (2020).

[12] Bjornsson, R. *et al.* Identification of a spin-coupled Mo(III) in the nitrogenase iron–molybdenum cofactor. *Chem. Sci.* **5**, 3096–3103 (2014).

[13] Bjornsson, R., Neese, F. & DeBeer, S. Revisiting the mössbauer isomer shifts of the FeMoco cluster of nitrogenase and the cofactor charge. *Inorg. Chem.* **56**, 1470–1477 (2017).

[14] Spiller, N., Bjornsson, R., DeBeer, S. & Neese, F. Carbon monoxide binding to the iron–molybdenum cofactor of nitrogenase: a detailed quantum mechanics/molecular mechanics investigation. *Inorg. Chem.* **60**, 18031–18047 (2021).

[15] Hohenberg, P. & Kohn, W. Inhomogeneous electron gas. *Phys. Rev.* **136**, B864–B871 (1964).

[16] Becke, A. D. Density-functional exchange-energy approximation with correct asymptotic behavior. *Phys. Rev. A* **38**, 3098–3100 (1988).

[17] Raugei, S., Seefeldt, L. C. & Hoffman, B. M. Critical computational analysis illuminates the reductive-elimination mechanism that activates nitrogenase for N_2 reduction. *Proc. Natl. Acad. Sci. U.S.A.* **115**, E10521–E10530 (2018).

[18] Hoeke, V. *et al.* High-resolution ENDOR spectroscopy combined with quantum chemical calculations reveals the structure of nitrogenase janus intermediate E4(4H). *J. Am. Chem. Soc.* **141**, 11984–11996 (2019).

[19] Lukoyanov, D. A. *et al.* Electron redistribution within the nitrogenase active site FeMo-Cofactor during reductive elimination of H_2 to achieve N_2 triple-bond activation. *J. Am. Chem. Soc.* **142**, 21679–21690 (2020).

[20] Cao, L. & Ryde, U. Putative reaction mechanism of nitrogenase after dissociation of a sulfide ligand. *J. Catal.* **391**, 247–259 (2020).

[21] Cao, L. & Ryde, U. N_2H_2 binding to the nitrogenase femo cluster studied by QM/MM methods. *BIC J. Biol. Inorg. Chem.* **25**, 521–540 (2020).

[22] Jiang, H., Svensson, O. K. G., Cao, L. & Ryde, U. Proton transfer pathways in nitrogenase with and without dissociated S2B. *Angew. Chem. Int. Ed.* (2022).

[23] Kästner, J. & Blöchl, P. E. Ammonia production at the FeMo cofactor of nitrogenase: Results from Density Functional Theory. *J. Am. Chem. Soc.* **129**, 2998–3006 (2007).

[24] Sippel, D. *et al.* A bound reaction intermediate sheds light on the mechanism of nitrogenase. *Science* **359**, 1484–1489 (2018).

[25] Bukas, V. J. & Nørskov, J. K. A molecular-level mechanism of the biological N_2 fixation. *ChemRxiv.* (2019).

[26] Li, Y. *et al.* H_2 formation holds the key to opening the Fe coordination sites of nitrogenase FeMo-cofactor for dinitrogen activation. *ChemRxiv.* (2020).

[27] Fraser, J. S. *et al.* Accessing protein conformational ensembles using room-temperature X-ray crystallography. *Proc. Natl. Acad. Sci. U.S.A.* **108**, 16247–16252 (2011).

[28] Li, W.-L. *et al.* Critical role of thermal fluctuations for CO binding on electrocatalytic metal surfaces. *JACS Au* **1**, 1708–1718 (2021).

[29] Li, W.-L. & Head-Gordon, T. Catalytic principles from natural enzymes and translational design strategies for synthetic catalysts. *ACS Cent. Sci.* **7**, 72–80 (2021).

[30] Welborn, V. V. & Head-Gordon, T. Fluctuations of electric fields in the active site of the enzyme ketosteroid isomerase. *J. Am. Chem. Soc.* **141**, 12487–12492 (2019).

[31] Hammes-Schiffer, S. Impact of enzyme motion on activity. *Biochemistry* **41**, 13335–13343 (2002).

[32] Bhowmick, A. & Head-Gordon, T. A Monte Carlo method for generating side chain structural ensembles. *Structure* **23**, 44–55 (2015).

[33] Offenbacher, A. R. *et al.* Hydrogen–Deuterium exchange of lipoxygenase uncovers a relationship between distal, solvent exposed protein motions and the thermal activation barrier for catalytic proton-coupled electron tunneling. *ACS Cent. Sci.* **3**, 570–579 (2017).

[34] Mardirossian, N. & Head-Gordon, M. Mapping the genome of meta-generalized gradient approximation density functionals: The search for B97M-V. *J. Chem. Phys.* **142**, 074111 (2015).

[35] Mardirossian, N. *et al.* Use of the rVV10 nonlocal correlation functional in the B97M-V density functional: Defining B97M-rV and related functionals. *J. Phys. Chem. Lett.* **8**, 35–40 (2017).

[36] Ruiz Pestana, L., Mardirossian, N., Head-Gordon, M. & Head-Gordon, T. Ab initio molecular dynamics simulations of liquid water using high quality meta-GGA functionals. *Chem. Sci.* **8**, 3554–3565 (2017).

[37] Mardirossian, N. & Head-Gordon, M. Thirty years of density functional theory in computational chemistry: an overview and extensive assessment of 200 density functionals. *Mol. Phys.* **115**, 2315–2372 (2017).

[38] Lininger, C. N. *et al.* Challenges for density functional theory: calculation of CO adsorption on electrocatalytically relevant metals. *Phys. Chem. Chem. Phys.* **23**, 9394–9406 (2021).

[39] Burgess, B. K. & Lowe, D. J. Mechanism of molybdenum nitrogenase. *Chem. Rev.* **96**, 2983–3012 (1996).

[40] Wilson, P., Nyborg, A. & Watt, G. Duplication and extension of the Thorneley and Lowe kinetic model for Klebsiella pneumoniae nitrogenase catalysis using a mathematica software platform. *Biophys. Chem.* **91**, 281–304 (2001).

[41] Hoffman, B. M., Lukoyanov, D., Dean, D. R. & Seefeldt, L. C. Nitrogenase: A draft mechanism. *Acc. Chem. Res.* **46**, 587–595 (2013).

[42] Cao, L., Caldararu, O. & Ryde, U. Protonation and reduction of the FeMo cluster in nitrogenase studied by quantum mechanics/molecular mechanics (QM/MM) calculations. *J. Chem. Theory Comput.* **14**, 6653–6678 (2018).

[43] Igarashi, R. Y. *et al.* Trapping H-bound to the nitrogenase FeMo-Cofactor active site during H_2 evolution: Characterization by ENDOR spectroscopy. *J. Am. Chem. Soc.* **127**, 6231–6241 (2005).

[44] Lukoyanov, D., Yang, Z.-Y., Dean, D. R., Seefeldt, L. C. & Hoffman, B. M. Is Mo involved in hydride binding by the four-electron reduced (E4) intermediate of the nitrogenase MoFe protein? *J. Am. Chem. Soc.* **132**, 2526–2527 (2010).

[45] Benton, P. M. C. *et al.* Localization of a substrate binding site on the FeMo-Cofactor in nitrogenase: Trapping propargyl alcohol with an alpha-70-substituted MoFe protein. *Biochemistry* **42**, 9102–9109 (2003).

[46] Lee, H.-I. *et al.* An organometallic intermediate during alkyne reduction by nitrogenase. *J. Am. Chem. Soc.* **126**, 9563–9569 (2004).

[47] Seefeldt, L. C., Hoffman, B. M. & Dean, D. R. Mechanism of Mo-dependent nitrogenase. *Annu. Rev. Biochem.* **78**, 701–722 (2009).

[48] Cao, L. & Ryde, U. Extremely large differences in DFT energies for nitrogenase models. *Phys. Chem. Chem. Phys.* **21**, 2480–2488 (2019).

[49] Cao, L. & Ryde, U. What is the structure of the E4 intermediate in nitrogenase? *J. Chem. Theory Comput.* **16**, 1936–1952 (2020).

[50] Van Stappen, C., Thorhallsson, A. T., Decamps, L., Bjornsson, R. & DeBeer, S. Resolving the structure of the E1 state of Mo nitrogenase through Mo and Fe K-edge EXAFS and QM/MM calculations. *Chem. Sci.* **10**, 9807–9821 (2019).

[51] Dance, I. How feasible is the reversible S-dissociation mechanism for the activation of FeMo-co, the catalytic site of nitrogenase? *Dalton Trans.* **48**, 1251–1262 (2019).

[52] Hammes-Schiffer, S. Theory of proton-coupled electron transfer in energy conversion processes. *Acc. Chem. Res.* **42**, 1881–1889 (2009).

[53] Hammes-Schiffer, S. Proton-coupled electron transfer: Moving together and charging forward. *J. Am. Chem. Soc.* **137**, 8860–8871 (2015).

[54] Lukoyanov, D. *et al.* Photoinduced reductive elimination of H_2 from the nitrogenase dihydride (Janus) state involves a FeMo-cofactor-H_2 intermediate. *Inorg. Chem.* **56**, 2233–2240 (2017).

[55] Thorhallsson, A. T., Benediktsson, B. & Bjornsson, R. A model for dinitrogen binding in the E4 state of nitrogenase. *Chem. Sci.* **10**, 11110–11124 (2019).

[56] Ohki, Y. *et al.* Nitrogen reduction by the fe sites of synthetic Mo_3S_4Fe cubes. *Nature* **7917**, 86–90 (2022).

[57] Wiberg, K. Application of the pople-santry-segal CNDO method to the cyclopropylcarbinyl and cyclobutyl cation and to bicyclobutane. *Tetrahedron* **24**, 1083–1096 (1968).

[58] Reed, A. E., Weinstock, R. B. & Weinhold, F. Natural population analysis. *J. Chem. Phys.* **83**, 735–746 (1985).

[59] Grunenberg, J. The interstitial carbon of the nitrogenase femo cofactor is far better stabilized than previously assumed. *Angew. Chem. Int. Ed.* **56**, 7288–7291 (2017).

[60] Maragliano, L., Fischer, A., Vanden-Eijnden, E. & Ciccotti, G. String method in collective variables: Minimum free energy paths and isocommittor surfaces. *J. Chem. Phys.* **125**, 024106 (2006).

[61] Cui, X., Tang, C. & Zhang, Q. A review of electrocatalytic reduction of dinitrogen to ammonia under ambient conditions. *Adv. Energy Mater.* **8**, 1800369 (2018).

[62] Li, X.-F. *et al.* Conversion of dinitrogen to ammonia by FeN_3-embedded graphene. *J. Am. Chem. Soc.* **138**, 8706–8709 (2016). PMID: 27383680.

[63] Welborn, V. V., Li, W.-L. & Head-Gordon, T. Interplay of water and a supramolecular capsule for catalysis of reductive elimination reaction from gold. *Nature Communications* **11**, 415 (2020).

[64] Perdew, J. P. Density-functional approximation for the correlation energy of the inhomogeneous electron gas. *Phys. Rev. B* **33**, 8822–8824 (1986).

[65] Goedecker, S., Teter, M. & Hutter, J. Separable dual-space gaussian pseudopotentials. *Phys. Rev. B* **54**, 1703–1710 (1996).

[66] Hartwigsen, C., Goedecker, S. & Hutter, J. Relativistic separable dual-space gaussian pseudopotentials from H to Rn. *Phys. Rev. B* **58**, 3641–3662 (1998).

[67] Li, W.-L., Chen, K., Rossomme, E., Head-Gordon, M. & Head-Gordon, T. Optimized pseudopotentials and basis sets for semiempirical density functional theory for electrocatalysis applications. *J. Phys. Chem. Lett.* **12**, 10304–10309 (2021).

[68] VandeVondele, J. & Hutter, J. Gaussian basis sets for accurate calculations on molecular systems in gas and condensed phases. *J. Chem. Phys.* **127**, 114105 (2007).

[69] VandeVondele, J. *et al.* Quickstep: fast and accurate density functional calculations using a mixed Gaussian and plane waves approach. *Comput. Phys. Commun.* **167**, 103–128 (2005).

[70] Hutter, J., Iannuzzi, M., Schiffmann, F. & VandeVondele, J. CP2K: atomistic simulations of condensed matter systems. *WIREs Comput. Mol. Sci.* **4**, 15–25 (2014).

[71] Frisch, M. J. *et al.* Gaussian09 revision E01 (2009). Gaussian Inc. Wallingford CT 2009.

[72] Curtiss, L. A. *et al.* Extension of Gaussian-2 theory to molecules containing third-row atoms Ga–Kr. *J. Chem. Phys.* **103**, 6104–6113 (1995).

[73] Dolg, M., Wedig, U., Stoll, H. & Preuss, H. Energy-adjusted ab initio pseudopotentials for the first row transition elements. *J. Chem. Phys.* **86**, 866–872 (1987).

[74] Martin, J. M. L. & Sundermann, A. Correlation consistent valence basis sets for use with the Stuttgart–Dresden–Bonn relativistic effective core potentials: The atoms Ga–Kr and In–Xe. *J. Chem. Phys.* **114**, 3408–3420 (2001).

[75] Seeger, R. & Pople, J. A. Self-consistent molecular orbital methods. XVIII. Constraints and stability in Hartree–Fock theory. *J. Chem. Phys.* **66**, 3045–3050 (1977).

[76] Bauernschmitt, R. & Ahlrichs, R. Stability analysis for solutions of the closed shell Kohn–Sham equation. *J. Chem. Phys.* **104**, 9047–9052 (1996).

[77] Barducci, A., Bussi, G. & Parrinello, M. Well-tempered metadynamics: A smoothly converging and tunable free-energy method. *Phys. Rev. Lett.* **100**, 020603 (2008).

[78] Barducci, A., Bonomi, M. & Parrinello, M. Metadynamics. *WIREs Comput. Mol. Sci.* **1**, 826–843 (2011).

AUTHOR CONTRIBUTIONS

W.L.L., Y.L. and T.H.G. designed the project. W.L.L. carried out the AIMD simulation, metadynamic calculation and performed bonding analyses. Y.L. determined the electronic structure and the scan curve calculation with the help of J.L.. All authors discussed the results and made comments and edits to the manuscript.

COMPETING INTERESTS

The authors declare no competing interests.

MATERIALS AND CORRESPONDENCE

Correspondence and material requests should be addressed to yong.li@kemi.uu.se and thg@berkeley.edu.

ACKNOWLEDGEMENTS

We thank the CPIMS program, Office of Science, Office of Basic Energy Sciences, Chemical Sciences Division of the U.S. Department of Energy under Contract DE-AC02-05CH11231 for support. This work used computational resources provided by the National Energy Research Scientific Computing Center (NERSC), a U.S. Department of Energy Office of Science User Facility operated under Contract DE-AC02-05CH11231. This work was also supported by the National Natural Science Foundation of China (NSFC grants 22033005, 21590792, and 91645203) and the Guangdong Key Laboratory of Catalytic Chemistry. We thank the Supercomputer centers at Tsinghua National Laboratory for Information Science and Technology and North-German Supercomputing Alliance (HLRN) for providing computational resources.

Supplementary Files

This is a list of supplementary files associated with this preprint. Click to download.

- NitrogenasesubmitSI.pdf